RAA 2021 Vol. **21** No. **1**, 8(12pp) doi: 10.1088/1674-4527/21/1/8
© 2021 National Astronomical Observatories, CAS and IOP Publishing Ltd.
http://www.raa-journal.org *http://iopscience.iop.org/raa*

Research in Astronomy and Astrophysics

An explanation for 13 consecutive day activities of Mrk 421

Yong-Gang Zheng[1,2,3,4], Chu-Yuan Yang[1,4], Shi-Ju Kang[5] and Jin-Ming Bai[1,4]

[1] Yunnan Observatories, Chinese Academy of Sciences, Kunming 650011, China;
ynzyg@ynu.edu.cn,baijinming@ynao.ac.cn
[2] Department of Physics, Yunnan Normal University, Kunming 650092, China
[3] Shandong Provincial Key Laboratory of Optical Astronomy and Solar-Terrestrial Environment-Shandong University, Weihai 264209, China
[4] Key Laboratory for the Structure and Evolution of Celestial Objects, Chinese Academy of Sciences, Kunming 650011, China
[5] Department of Physics and Electronics Science, Liupanshui Normal University, Liupanshui 553004, China

Received 2020 April 8; accepted 2020 July 17

Abstract It is surprising to find an instance of migration in the peak positions of synchrotron spectral energy distribution components during the activity epochs of Markarian 421 (Mrk 421), accompanying an orphan flare at the X-ray and GeV-TeV γ-ray bands. A geometric interpretation and standard shock or stochastic acceleration models of blazar emission have difficulty reproducing these observed behaviors. The present paper introduces a linear acceleration by integrating the reconnection electric field into the particle transport model for the observed behaviors of Mrk 421. We note that strong evidence for evolution in characteristic of multi-wavelength spectral energy distribution including shifting the peak frequency, accompanying an orphan flare at the X-ray and GeV-TeV γ-ray bands provides an important electrostatic acceleration diagnostic in a blazar jet. Assuming suitable model parameters, we apply the results of the simulation to the 13-day flaring event in March 2010 of Mrk 421, concentrating on the evolution of multi-wavelength spectral energy distribution characteristic by shifting the peak frequency. It is clear that the ratio of the electric field and magnetic field strength plays an important role in temporal evolution of the peak frequency of synchrotron spectral energy distribution component. We suggest it is reasonable that the electrostatic acceleration is responsible for the evolution of multi-wavelength spectral energy distribution characteristic by shifting the peak frequency. Based on the model results, we assert that the peak frequency of the synchrotron spectral energy distribution component may signify a temporary characteristic of blazars, rather than a permanent one.

Key words: radiation mechanisms: non-thermal — BL Lacertae objects: individual: (Mrk 421) — acceleration of particles

1 INTRODUCTION

Blazars are radio-loud active galactic nuclei (AGNs). In the most accepted scenario, their continuum emissions extending from radio to γ-ray bands arise from the relativistic jet. This jet emerges from supermassive black holes and beams the emission at the observer's line of sight (e.g., Ghisellini et al. 1986; Urry & Padovani 1995). Hence, the observed spectra are subjected to the effects of Doppler boosting (Blandford & Königl 1979). In general, multi-wavelength observations show the spectral energy distribution (SED) of blazars in $\log\nu - \log\nu F_\nu$ space exhibits a double-peak shape (Fossati et al. 1998). It is believed that the low-energy peak of the SED is attributed to synchrotron emission from extreme relativistic electrons and/or positrons in the jet (Urry 1998). The origin of the high-energy component remains an open issue. The lepton model suggests that it may be attributed to the inverse Compton (IC) scattering of extremely relativistic electrons (e.g., Jones et al. 1974; Ghisellini & Maraschi 1989; Dermer et al. 1992; Zheng & Yang 2016; Zheng et al. 2017).

Most blazars appear as luminous sources characterized by noticeable and rapid flux variability at all observed frequencies. Generally, prominent X-ray and γ-ray flares tend to be correlated with low frequency flares (e.g., Raiteri et al. 2017). Due to observational limitations, it is difficult to obtain a detailed picture of the time-varying emission spectrum. Previous efforts to study the temporary spectrum from a blazar have concentrated mainly on the production of variability via either time-dependent particle distribution (e.g., Bloom & Marscher 1996; Chiaberge & Ghisellini 1999; Böttcher & Chiang 2002; Katarzyński et al. 2006; Zheng & Zhang 2011; Weidinger & Spanier 2015; Lewis et al. 2016) or some physical (e.g., Blandford & Königl 1979; Marscher & Gear 1985; Celotti et al. 1991; Mastichiadis & Kirk 1997; Kirk et al. 1998; Giebels et al. 2007; Mastichiadis & Moraitis 2008) and/or geometrical parameters changing (e.g., Camenzind & Krockenberger 1992; Gopal-Krishna & Wiita 1992). In recent years, the unprecedented study of multi-wavelength observation campaigns obtained the spectra of blazars as close in time as possible (e.g., Aleksić et al. 2015; Baloković et al. 2016; Kataoka & Stawarz 2016; Abeysekara et al. 2017; Ahnen et al. 2018). While models endeavor to describe the temporary characteristics of the emission spectrum (Aleksić et al. 2015; Baloković et al. 2016), migration in the peak positions of the synchrotron emission SED component during activity epochs remains an open issue.

Both the diffusive shock acceleration (e.g., Bell 1978; Drury 1983; Marscher 2014; Zheng et al. 2018) and stochastic acceleration (e.g., Schlickeiser 1985, 1989; Petrosian & Liu 2004; Zheng & Zhang 2011; Asano & Hayashida 2015; Baring et al. 2017) are potentially efficient mechanisms for producing energetic particles from a plasma flow with strong shocks. In spite that the mechanisms, including the injection, acceleration and cooling of particles (Ghisellini et al. 2002), with the possible intervention of shock waves (Marscher & Gear 1985; Sikora et al. 2001) or turbulence (Marscher 2014), are still being debated in terms of producing the unpredictable variability, previous model efforts can simulate the properties of these flares (e.g., Zheng & Zhang 2011; Nalewajko et al. 2012; Petropoulou 2014). There is a class of γ-ray flares that occurs with little correlated variability that is detected at longer wavelengths (e.g., Krawczynski et al. 2004; Rani et al. 2013). Since the theoretical photon spectra reproducing standard shock or stochastic acceleration models are calculated in the synchrotron self-Compton (SSC) model frame, it is difficult for the mentioned models to explain this pure orphan flare. For the purpose of applying a proposed model, in this context we expand the orphan flare to include the flares at both X-ray and γ-ray bands.

It is generally believed that the magnetohydrodynamic (MHD) instabilities of a Poynting-flux dominated plasma flow result in formation of current sheets where the magnetic reconnection is triggered (Eichler 1993; Begelman 1998; Giannios & Spruit 2006). Particle acceleration in reconnection has been used to interpret the prompt phenomena of γ-ray bursts (e.g., Beniamini & Piran 2013; Zhang & Zhang 2014; Beniamini & Granot 2016; Beniamini & Giannios 2017), in addition to the high-energy non-thermal emission from pulsar wind nebulae (e.g., Kirk & Skjæraasen 2003; Cerutti et al. 2012, 2013; Philippov & Spitkovsky 2014; Cerutti & Philippov 2017) and AGN jets (e.g., Romanova & Lovelace 1992; Giannios et al. 2009, 2010; Nalewajko et al. 2011; Narayan & Piran 2012; Giannios 2013; Petropoulou et al. 2016; Christie et al. 2019). While the particle-in-cell (PIC) simulations (Sironi & Spitkovsky 2014; Guo et al. 2014; Werner & Uzdensky 2017) reveal several difficulties in understanding how the reconnection produces efficient particle acceleration, one can suggest that linear acceleration by the reconnecting electric field is the simplest and most fundamental acceleration mechanism (Kagan et al. 2018). In principle, magnetic reconnection offers natural locations, within the diffusion region where the magnetic field is small and reverse, in which the electric field can exceed the magnetic field (Cerutti et al. 2013). These results indicate the electrostatic acceleration can drive up the particle energy to a level that significantly overruns the possible values when only the shock and stochastic acceleration are considered. In these scenarios, we anticipate extreme incident behavior in the quasi-spherical emission region of the blazar jet to occur.

In the present context, we attempt to account for the temporary characteristic of the emission spectrum by introducing an electrostatic acceleration mechanism. The aim of this paper is to find the distinctive energy spectrum characteristics for the electrostatic acceleration in the blazar jet. The present paper is organized as follows. In Section 2, we take the rate of the linear electrostatic acceleration into account in the model by assuming a constant electric field strength. In Section 3, we discuss the model parameters and establish a ratio for the electric field and the magnetic field strengths reflecting the electrostatic acceleration rate. In Section 4, we estimate the maximum Lorentz factor of the particles in the model. Based on the expected maximum Lorentz factor, we deduce the maximum energy of the synchrotron peak, and we propose an important electrostatic acceleration diagnostic in the blazar jet. In Section 5, we apply the model to the 13-day flaring event in March 2010 of Markarian 421 (Mrk 421). This application concentrates on the electrostatic acceleration responsible for the evolution of the multi-wavelength SED characteristic by shifting the peak frequency; a discussion is given in Section 6.

Throughout the paper, all of the parameters are calculated in the comoving frame. Then, we transfer them from the comoving frame to the observed frame by taking relativistic beaming effect into account. We assume the Hubble constant $H_0 = 75\ \mathrm{km\,s^{-1}\,Mpc^{-1}}$, the dimensionless numbers for the energy density of matter $\Omega_{\rm M} = 0.27$, the dimensionless numbers of radiation energy density $\Omega_{\rm r} = 0$ and the dimensionless cosmological constant $\Omega_\Lambda = 0.73$.

2 THE PROPOSED MODEL

The photon spectra in the current context are calculated by the model within the lepton model frame through both synchrotron emission and IC scattering. In the proposed model, we basically follow the approach of Zheng et al. (2019) to calculate the electron spectrum, and we introduce electrostatic acceleration to the first-order gain rate. In our approaches, since magnetic reconnections occur in a natural location, we do not take the actual electrostatic acceleration process. Phenomenologically, we treat the electrostatic acceleration as a mechanism to gain energy in the transport equation, that is, the electrons pick up energy from the electric fields.

Assuming an electric field of strength E is generated in the magnetic reconnection region around the shock, we estimate the electrostatic acceleration rate experienced by the electrons with the magnitude of the electron charge, e, due to the electric field crossing in the comoving frame as follows

$$\dot{p}_{\rm elec} = eE\,. \tag{1}$$

Combining the momentum gain rate with shock acceleration, $\dot{p}_{\rm sh}$, we can establish the first-order momentum gain rate

$$\dot{p}_{\rm gain} = \dot{p}_{\rm elec} + \dot{p}_{\rm sh} = A_0 m_e c\,, \tag{2}$$

where A_0 is the first-order momentum gain rate constant in the unit of $\mathrm{s^{-1}}$ with $A_0 = A_{\rm sh} + A_{\rm elec}$, m_e the electron mass and c the speed of light. In this scenario, we rebuild the basic transport equation as follows

$$\begin{aligned}\frac{\partial f(p,t)}{\partial t} = {} & \frac{1}{p^2}\frac{\partial}{\partial p}\left\{p^2\left[D_0 m_e c p\frac{\partial f(p,t)}{\partial p} - A_0 m_e c f(p,t)\right.\right.\\ & \left.\left. + \frac{B_0 p^2}{m_e c} f(p,t)\right]\right\} - \left(\frac{C_0 m_e c}{p} + \frac{F_0 p}{m_e c}\right) f(p,t)\\ & + \frac{\dot{N}_0 \delta(p-p_0)}{4\pi p_0^2}\,,\end{aligned} \tag{3}$$

where $f(p,t)$ is the isotropic, homogeneous phase-space density, p is the particle momentum, D_0 is the momentum diffusion rate constant, B_0 is the momentum-loss rate constant, C_0 is the shock-regulated escape rate constant, F_0 is the Bohm diffusive escape rate constant, $\dot{N}_0$ is the continual injection rate in the units of $p^{-1}\mathrm{cm^{-3}\,s^{-1}}$, p_0 is the characteristic injection momentum and $\delta(p)$ is Dirac's distribution function.

Using a Green's function to solve the stationary particle transport equation (see e.g., Kroon et al. 2016; Zheng et al. 2019), we can obtain the closed-form solution for the electron Green's function, $N_G(\gamma,\gamma_0)$, representing the number density distribution of electrons in the Lorentz factor, γ, space with the Gamma function, $\Gamma(x)$, as follows

$$\begin{aligned}N_G(\gamma,\gamma_0) = {} & \frac{\dot{N}_0 m_e c \Gamma(\mu-\sigma+0.5)}{\hat{B} D_0 \Gamma(1+2\mu)\gamma_0^2}\left(\frac{\gamma}{\gamma_0}\right)^{\frac{\hat{A}}{2}}\\ & \times e^{-\frac{\hat{B}(\gamma^2-\gamma_0^2)}{4}} M_{\sigma,\mu}\Big(\frac{\hat{B}\gamma_1^2}{2}\Big) W_{\sigma,\mu}\Big(\frac{\hat{B}\gamma_2^2}{2}\Big)\,,\end{aligned} \tag{4}$$

where we let $\hat{A} = A_0/D_0$, $\hat{B} = B_0/D_0$, $\hat{C} = C_0/D_0$ and $\hat{F} = F_0/D_0$. The model assumes that the injected particles have a mono-energetic distribution, and the parameter γ_0 is a characteristic Lorentz factor of the injected particles. The Whittaker functions $M_{\sigma,\mu}(\frac{\hat{B}\gamma_1^2}{2})$ and $W_{\sigma,\mu}(\frac{\hat{B}\gamma_2^2}{2})$ are defined by the parameter $\sigma = 1 + \hat{A}/4 - \hat{F}/(2\hat{B})$, and $\mu = 0.25[(2+\hat{A})^2 + 4\hat{C}]^{1/2}$ with $\gamma_1 = \min[\gamma,\gamma_0]$ and $\gamma_2 = \max[\gamma,\gamma_0]$.

We can utilize the number density distribution of electrons determined by Equation (4) to calculate the emission intensity of the synchrotron radiation, $I_{\rm syn}(\nu)$, and the IC scattering, $I_{\rm ic}(\nu)$ in the SSC model frame (e.g., Katarzyński et al. 2001; Zheng et al. 2019). Taking the absorption effect of the extragalactic background light (EBL) into account, we can calculate the flux density at Earth (e.g., Zheng & Zhang 2011)

$$\begin{aligned}F_{\rm obs.}(\nu_{\rm obs.}) = {} & \frac{\pi\delta^3(1+z)r_s^2}{d_L^2}\Big[I_{\rm syn}(\nu) + I_{\rm ic}(\nu)\Big]\\ & \times e^{-\tau(\nu,z)}\,,\end{aligned} \tag{5}$$

where δ is the Doppler factor (e.g., Rybicki & Lightman 1979), z the redshift of the source, r_s the size of the blob, d_L the luminosity distance and $\tau(\nu,z)$ the absorption optical depth (e.g., Dwek & Krennrich 2005). The relationship between the frequency, $\nu_{\rm obs.}$, at observer's frame and the frequency, ν, at comoving frame is given by $\nu_{\rm obs.} = \delta\nu/(1+z)$.

3 THE MODEL PARAMETERS

The application of the model requires the specification of both the particle spectral parameters (i.e., $\dot{N}_0$, D_0, γ_0, $\hat{A}$, $\hat{B}$, $\hat{C}$ and $\hat{F}$), and the jet parameters (B, δ and r_s). Since we introduce electrostatic acceleration to the first-order gain rate, we should reestablish the parameter relationships, rather than relying on the model parameters determined in our early work. Based on the equations presented by Zheng et al. (2019) and Equations (1) and (2) in the current context, we find

$$\hat{A} = \hat{A}_{\rm sh} + \hat{A}_{\rm elec} = \frac{9\eta\xi}{4\sigma_{\rm mag}} + \frac{E}{B}\frac{3\eta}{\sigma_{\rm mag}} \,, \tag{6}$$

$$\hat{B} = 5.54\times10^{-13}\frac{\eta u}{\sigma_{\rm mag}}(\frac{B}{0.1\ {\rm G}})^{-1} \,, \tag{7}$$

$$\hat{C} = \frac{3\eta}{\omega\sigma_{\rm mag}} \,, \tag{8}$$

and

$$\hat{F} = 8.74\times10^{-26}\eta^2\sigma_{\rm mag}^{-1}(\frac{r_s}{10^{17}\ {\rm cm}})^{-2}(\frac{B}{0.1\ {\rm G}})^{-2} \,, \tag{9}$$

where η is a dimensionless parameter, ξ is the efficiency factor of shock acceleration, $\sigma_{\rm mag}$ is the magnetization parameter, B is the local magnetic field strength, u is the summation of both the magnetic field and the soft photon field energy density and ω is a dimensionless constant of order unity.

In our proposed approach, we require increasing the summation of both the magnetic field and the soft photon field energy density as free particle spectral parameters; this is based on the free parameters of Zheng et al. (2019). Once the values of particle spectral parameters are established, we can derive the momentum diffusion rate constant as follows,

$$D_0 = \frac{4\sigma_T u}{3m_e c\hat{B}} \,, \tag{10}$$

where σ_T is the Thomson cross section, the magnetization parameter, $\sigma_{\rm mag}$, is

$$\sigma_{\rm mag} = \frac{3\eta D_0 m_e c}{eB} \,, \tag{11}$$

and the dimensionless timescale constant, ω, is as follows

$$\omega = \frac{3\eta}{\hat{C}\sigma_{\rm mag}} \,. \tag{12}$$

Next, we can obtain the averaged soft photon field, $u_{\rm ph}$, with

$$u_{\rm ph} = u - \frac{B^2}{8\pi} \,, \tag{13}$$

and the ratio of the electric field and magnetic field strength, E/B, as follows

$$\frac{E}{B} = \frac{\hat{A}\sigma_{\rm mag}}{3\eta} - \frac{3}{4}\xi \,. \tag{14}$$

4 RADIATION ENERGY OF MAXIMUM PARTICLES

The transport equation in the current context takes the shock, electrostatic, stochastic acceleration, synchrotron and IC scattering losses, as well as particle injection and escape into account. A dynamic equilibrium is generated by a kind of competition among the acceleration, cooling, injection and escape of particles from the shock region. Neglecting the particle injection and escape, we can estimate the maximum Lorentz factor of the particles, $\gamma_{\rm max}$, by examining the Fokker-Plank "drift" coefficient, $\langle dp/dt\rangle = D_0 m_e c(3+\hat{A}-\hat{B}\gamma_{\rm max}^2) = 0$, which yields

$$\gamma_{\rm max}^2 = \gamma_{\rm e,stoch}^2 + \gamma_{\rm e,sh}^2 + \gamma_{\rm e,elec}^2 \,. \tag{15}$$

It is convenient to obtain the theoretical equilibrium momentum for a combination of stochastic acceleration and momentum loss by balancing the stochastic momentum gain rate, $\dot{p}_{\rm stoch}$, with the momentum-loss rate, $\dot{p}_{\rm loss}$, so that the equation

$$(\dot{p}_{\rm stoch} + \dot{p}_{\rm loss})|_{p=p_{\rm e,stoch}} = 0 \tag{16}$$

can be established. The equilibrium Lorentz factor for stochastic acceleration versus momentum loss is therefore expressed as

$$\gamma_{\rm e,stoch} = \frac{p_{\rm e,stoch}}{m_e c} = \sqrt{\frac{9D_0 m_e c}{4\sigma_T u}} \,. \tag{17}$$

With the same approach, we can establish the following equations

$$(\dot{p}_{\rm sh} + \dot{p}_{\rm loss})|_{p=p_{\rm e,sh}} = 0 \,, \tag{18}$$

and

$$(\dot{p}_{\rm elec} + \dot{p}_{\rm loss})|_{p=p_{\rm e,elec}} = 0 \,, \tag{19}$$

which yield the equilibrium Lorentz factor for shock acceleration versus momentum loss,

$$\gamma_{\rm e,sh} = \frac{p_{\rm e,sh}}{m_e c} = \sqrt{\frac{9\xi eB}{16\sigma_T u}} \,, \tag{20}$$

and the equilibrium Lorentz factor for electrostatic acceleration versus momentum loss,

$$\gamma_{\rm e,elec} = \frac{p_{\rm e,elec}}{m_e c} = \sqrt{\frac{3eE}{4\sigma_T u}} \,. \tag{21}$$

The Larmor timescale is the minimum timescale for acceleration of the particles via energetic collisions with MHD waves,

$$t_{\rm L}(p) = \frac{r_{\rm L}}{c} = \frac{p}{eB} \,, \tag{22}$$

where $r_{\rm L}$ is the Larmor radius. Equating the Larmor timescale with the timescale of momentum loss

$$[t_{\rm L}(p) + t_{\rm loss}(p)]|_{p=p_{\rm MHD}} = 0 \,, \tag{23}$$

yields a critical Lorentz factor,

$$\gamma_{\rm MHD} = \frac{p_{\rm MHD}}{m_e c} = \sqrt{\frac{3eB}{4\sigma_T u}} \,. \tag{24}$$

Since both shock and stochastic acceleration are mediated by interactions between the electrons and the MHD wave, we expect neither the $\gamma_{\rm e,stoch}$ nor the $\gamma_{\rm e,sh}$ to exceed the critical Lorentz factor, $\gamma_{\rm MHD}$. These assumptions give

$$D_{0,\rm max} = \frac{eB}{3m_e c} \,, \tag{25}$$

and $\xi_{\rm max} = 4/3$. On the other hand, we infer that the combination of these two processes cannot accelerate an electron with a Lorentz factor that exceeds the critical Lorentz factor, that is

$$(\dot{p}_{\rm stoch} + \dot{p}_{\rm sh} + \dot{p}_{\rm loss})|_{p=p_{\rm MHD}} \le 0 \,. \tag{26}$$

This relation yields

$$(\frac{D_0}{D_{0,\rm max}} + \frac{3}{4}\xi) \le 1 \,. \tag{27}$$

Substituting Equations (17), (20), (21) and (25) into Equation (15) yields

$$\begin{aligned}\gamma_{\rm max} &= \sqrt{\frac{3eB}{4\sigma_T u}(\frac{D_0}{D_{0,\rm max}} + \frac{3}{4}\xi + \frac{E}{B})} \\ &= 7.36\times 10^7 \left(\frac{B}{0.1\ \rm G}\right)^{1/2} \left(\frac{u}{0.01\ \rm erg\ cm^{-3}}\right)^{-1/2} \\ &\times \left(\frac{D_0}{D_{0,\rm max}} + \frac{3}{4}\xi + \frac{E}{B}\right)^{1/2} \,.\end{aligned} \tag{28}$$

The characteristic energy of the synchrotron emission peak is (e.g., Rybicki & Lightman 1979)

$$\begin{aligned}E_{\rm syn,peak}(\gamma) &= \gamma^2 m_e c^2 \frac{B}{B_{\rm crit}} \\ &= 0.12\ {\rm MeV} \left(\frac{\gamma}{10^7}\right)^2 \left(\frac{\rm B}{0.1\ \rm G}\right) \,,\end{aligned} \tag{29}$$

where $B_{\rm crit}$ is critical magnetic field with $B_{\rm crit} = 4.41 \times 10^{13}$ G. We can substitute Equation (28) into Equation (29) to obtain the photon energy of the synchrotron peak, given by

$$\begin{aligned}E_{\rm syn,peak}(\gamma_{\rm max}) &= \gamma_{\rm max}^2 m_e c^2 \frac{B}{B_{\rm crit}} \\ &= 6.50\ {\rm MeV} \left(\frac{\rm B}{0.1\ \rm G}\right)^2 \left(\frac{\rm u}{0.01\ \rm erg\ cm^{-3}}\right)^{-1} \\ &\times \left(\frac{D_0}{D_{0,\rm max}} + \frac{3}{4}\xi + \frac{E}{B}\right) \,.\end{aligned} \tag{30}$$

Substituting Equation (27) into Equation (30) yields

$$\begin{aligned}E^{\rm max}_{\rm syn,peak}(\gamma_{\rm max}) &\le 6.50\ {\rm MeV} \left(\frac{\rm B}{0.1\ \rm G}\right)^2 \\ &\times \left(\frac{u}{0.01\ \rm erg\ cm^{-3}}\right)^{-1} \left(1 + \frac{E}{B}\right) \,.\end{aligned} \tag{31}$$

Equation (31) indicates that the maximum photon energy of the synchrotron peak, $E^{\rm max}_{\rm syn,peak}(\gamma_{\rm max})$ depends on the magnetic field strength, B, radiation field energy density, $u_{\rm ph}$, and electric field strength, E.

It is important to note that we can employ the three most common approaches to explain the evolution of the multi-wavelength SED characteristic by shifting the peak frequency. The three approaches are (1) varying the magnetic field strength; (2) varying the radiation field energy density; and (3) varying the electric field strength. As can be seen in Equations (10) and (14), regardless of changing either the magnetic field strength or the radiation field energy density, these changes result in a substantial influence on the value of the electrostatic field in the proposed model in the current context. The changes in the multi-wavelength SED as a result of varying the physical parameters B, u and $\hat{A}$ are plotted in Figure 1. One can see that the migration in the peak positions of the synchrotron SED component dominates in the evolution of the multi-wavelength SED. Phenomenologically, we anticipate that some incidental behaviors can be expected from the emission spectra. Neglecting the influence on the other physical conditions, if we focus on varying either the magnetic field strength or the radiation field energy density, since the dynamic equilibrium of the system reestablishes, we can find a continuous variability covering energies from high to low. Alternatively, if we focus on varying the electric field strength, because the acceleration efficiency relies on the electron populations around the equilibrium energy, we can expect the shapes of these SED bumps to change. In addition, the flux variability is remarkable and the change of spectral slopes is significant at the X-ray and GeV-TeV γ-ray bands; however, as a result of the low energy electrons being dominated by the electrostatic acceleration process, the variability is minor or not significant at the low frequency end of the synchrotron component. In these scenarios, we assert that there is strong evidence for the evolution of the multi-wavelength characteristic SED by shifting the peak frequency, and this is accompanied by an orphan flare at the X-ray and GeV-TeV γ-ray bands. Consequently, these observations provide an important electrostatic acceleration diagnostic in blazar jets.

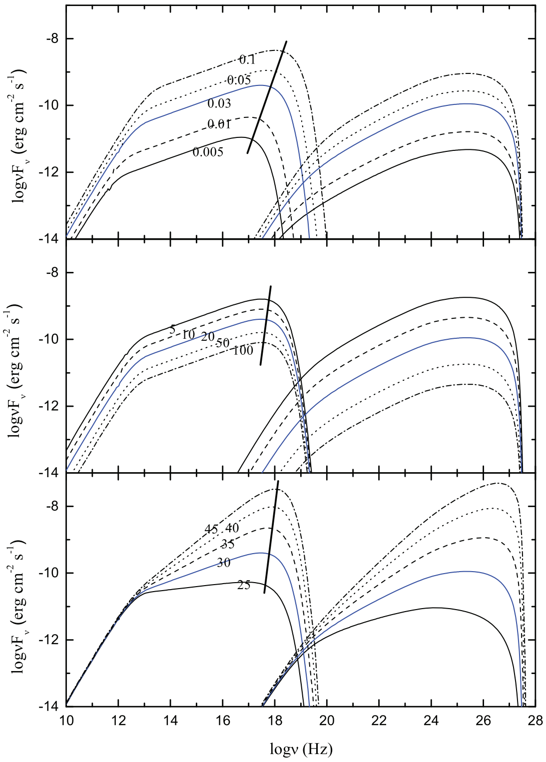

Fig. 1 The changes in the multi-wavelength SED by varying the physical parameters. The *top panel* features the magnetic field strength B, the *middle panel* displays the summation of both the magnetic field and the soft photon field energy density u, which indicates the varying radiation field energy density, $u_{\rm ph}$, when the parameter B is fixed. The *bottom panel* depicts the dimensionless parameter $\hat{A}$, which indicates the varying ratio of the electric field and magnetic field strength, E/B, when the parameters B and u are fixed. The labels near the curves signify the values of the parameter. The *thick lines* are plotted by the peak frequency of the synchrotron SED component. The *blue curve* marks the baseline of the multi-wavelength SED with the chosen parameters $\gamma_0 = 1000$, $\dot{N}_0 = 2.0 \times 10^{19}$ p^{-1} cm^{-3} s^{-1}, $\xi = 0.1$, $\eta = 1$, $u = 20$ erg cm^{-3}, $\hat{A} = 30$, $\hat{B} = 8.54 \times 10^{-11}$, $\hat{C} = 84$, $\delta = 32$, $B = 0.03$ G and $r_s = 2.1 \times 10^{16}$ cm.

5 APPLICATION TO MRK 421

Mrk 421 is a nearby active galaxy at a redshift of $z = 0.031$ (de Vaucouleurs et al. 1991), with a pair of relativistic jets flowing in opposite directions that are closely aligned to our line of sight. It is interesting to find the significant evolution of the multi-wavelength SED characteristic by shifting the peak frequency that has been exhibited during activity epochs (e.g., Ushio et al. 2010; Aleksić et al. 2015; Baloković et al. 2016). During these epochs, the archival multi-wavelength observations of Mrk 421 show the synchrotron and the IC scattering peak in the quiescent state located at ~ 1 keV and ~ 100 GeV, respectively (e.g., Abdo et al. 2011). On the other hand, the 13 consecutive day (from MJD 55265 to MJD 55277) activity of Mrk 421 occurring in March 2010 manifests an orphan flare at the X-ray and GeV-TeV γ-ray bands (Aleksić et al. 2015).

In order to attempt to understand the nature of the migration in the peak positions of the SED, in the current context, we apply the proposed model to the 13-day flaring event in March 2010 of Mrk 421, concentrating on the electrostatic acceleration responsible for the evolution of multi-wavelength SED characteristic by shifting the peak frequency. We first establish the values of the model parameters. Our approach for reproducing the multi-wavelength spectrum from Mrk 421 sets $\eta = 1$, $\xi = 0.1$ and $\delta = 32$ in all of the observation epochs. Since the adopted multi-wavelength SEDs are averaged daily, we argue that our approximation is valid as long as the variability timescale, $t_{\rm var}$, is less than 1-day. In this scenario, we constrain the size of the emission region by the relation $r_s \sim c\delta t_{\rm var}/(1+z) = 2.1 \times 10^{16}$ cm with $t_{\rm var} = 2.25 \times 10^4$ s in all of the calculation epochs. The other model parameters $\dot{N}_0$, γ_0, $\hat{A}$, $\hat{B}$, $\hat{C}$, u and B are varied until a reasonable qualitative fit to the multi-wavelength spectral data is obtained.

In Figure 2, we plot the model spectrum along with the simultaneous multi-wavelength SED observations reported by Aleksić et al. (2015) in the epoch of March 2010 from Mrk 421. The plots include a comparison of the nonflaring (or typical) SED from the 2009 MW campaign observed in Abdo et al. (2011). The corresponding physical parameters of the model spectrum for the 13-day flaring event in March 2010 and the nonflaring state of Mrk 421 are reported in Table 1. We can estimate the specific amount of the shock and the electric field by using $\hat{A}_{\rm sh} = 9\eta\xi/(4\sigma_{\rm mag})$ and $\hat{A}_{\rm elec} = 3E\eta/(B\sigma_{\rm mag})$. The results are also listed in Table 1. We can see that the electrostatic acceleration dominates in activities during the 13 consecutive days. The inferred values of electric field in the reconnection layer are also included in Table 1. It can be seen that, for the strong flares at the beginning of the activity epochs, the condition $E \gtrsim B$ is in accord with rapid magnetic reconnection, which can result in efficient electrostatic acceleration. The exceptions are the tear of flare activity. For these weak flares, we obtain $E < B$. Since the intensities of these particular flare activities barely exceeded the level of the quiescent emission, we assert that the results are reasonable in the sense that strong electrostatic acceleration is not required to interpret the spectrum observed during those 13 consecutive day activities.

We now take the evolution of the multi-wavelength SED characteristic into account by shifting the peak fre-

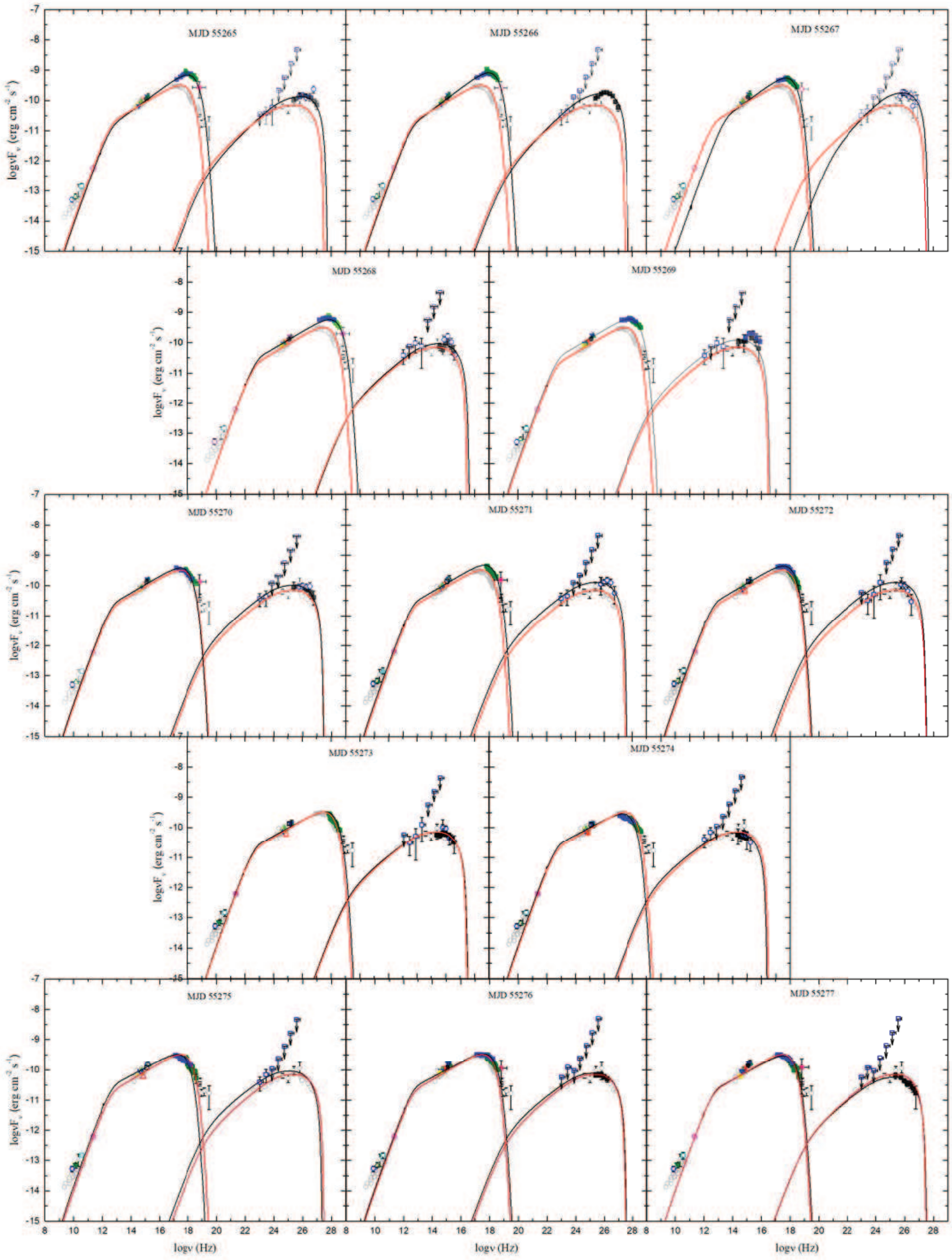

Fig. 2 Comparisons of model spectra with observed data for the BL Lac object Mrk 421. The colored symbols indicate the daily SEDs during 13 consecutive days (from MJD 55262 to MJD 55277) of activity taken from Aleksić et al. (2015). The Fermi upper limits are displayed as *blue open squares* with down arrows. The *gray circles* in the background of each panel signify the averaged SED from the 2009 MW campaign reported in Abdo et al. (2011), which is a good representation of the nonflaring SED of Mrk 421. The model-derived spectra that fit the daily SEDs are plotted with *red curves* in each panel, while spectra that fit the nonflaring SED are plotted with *black curves*.

quency. Since very high-energy (VHE) photons, in general $E_\gamma > 0.1$ TeV, from the source are attenuated by photons from the EBL (e.g., Stecker et al. 1992; Kneiske et al. 2002, 2004; Dwek & Krennrich 2005; Stecker et al. 2006; Franceschini et al. 2008; Razzaque et al. 2009; Finke et al. 2010), we deduce that the peak position of the high-energy SED component from Mrk 421 depends on the $\gamma\gamma$ attenuation effect. In this scenario, we do not consider the peak position of the IC scattering SED component; instead, we estimate the peak location of the syn-

Table 1 The Proposed Model Parameters

Date MJD	$\dot{N}_0$ [$\mathrm{p^{-1}\,cm^{-3}\,s^{-1}}$]	γ_0 ...	ξ ...	η ...	$\hat{A}$ ...	$\hat{B}$ [10^{-11}]	$\hat{C}$ ...	u [$\mathrm{erg\,cm^{-3}}$]	B [G]	δ ...	r_s [10^{16} cm]	$\hat{F}$ [10^{-22}]	D_0 [$\mathrm{s^{-1}}$]	σ_{mag} ...	ω ...	E [G]	$\hat{A}_{\mathrm{sh}}$ ...	$\hat{A}_{\mathrm{elec}}$ ...
typical	2.0×10^{19}	1000	0.1	1.0	30	8.54	84.0	25.38	0.030	32	2.1	4.01	9.65×10^{3}	0.055	0.65	0.014	4.103	25.92
55265	3.5×10^{19}	1000	0.1	1.0	20	2.54	56.0	25.38	0.030	32	2.1	1.19	3.24×10^{4}	0.185	0.29	0.035	1.222	18.82
55266	3.5×10^{19}	1000	0.1	1.0	19	2.54	53.2	25.38	0.030	32	2.1	1.19	3.24×10^{4}	0.185	0.31	0.033	1.222	17.82
55267	3.0×10^{18}	3000	0.1	1.0	20	2.54	56.0	25.38	0.023	32	2.1	2.15	2.35×10^{4}	0.175	0.31	0.025	1.292	18.76
55268	3.2×10^{19}	1000	0.1	1.0	30	4.50	84.0	25.38	0.040	32	2.1	1.59	1.83×10^{4}	0.078	0.46	0.028	2.885	27.16
55269	3.2×10^{19}	1000	0.1	1.0	30	5.50	84.0	25.38	0.038	32	2.1	2.04	1.50×10^{4}	0.067	0.53	0.023	3.347	26.67
55270	2.2×10^{19}	1000	0.1	1.0	30	9.50	84.0	25.38	0.030	32	2.1	4.46	8.68×10^{3}	0.049	0.72	0.012	4.562	25.44
55271	4.0×10^{19}	1000	0.1	1.0	30	5.50	84.0	25.38	0.030	32	2.1	2.58	1.50×10^{4}	0.085	0.42	0.023	2.642	27.37
55272	3.0×10^{19}	1000	0.1	1.0	30	7.50	84.0	25.38	0.030	32	2.1	3.52	1.10×10^{4}	0.063	0.57	0.016	3.603	26.42
55273	2.8×10^{19}	1000	0.1	1.0	35	7.50	98.0	25.38	0.032	32	2.1	3.30	1.10×10^{4}	0.059	0.52	0.019	3.843	31.18
55274	1.6×10^{19}	1000	0.1	1.0	37	15.0	103.6	25.38	0.032	32	2.1	6.61	5.49×10^{3}	0.029	0.98	0.009	7.694	29.37
55275	1.6×10^{19}	1000	0.1	1.0	37	18.0	103.6	25.38	0.032	32	2.1	7.93	4.58×10^{3}	0.024	1.19	0.007	9.223	27.80
55276	3.1×10^{19}	1000	0.1	1.0	37	8.0	103.6	25.38	0.032	32	2.1	3.52	1.03×10^{4}	0.055	0.53	0.019	4.101	32.94
55277	2.4×10^{19}	1000	0.1	1.0	35	8.0	98.0	25.38	0.032	32	2.1	3.52	1.03×10^{4}	0.055	0.56	0.018	4.101	30.94

Table 2 Results of the Log-parabolic Model[a] to Fit the X-ray Data alone, and both the UV/Optical and X-ray Data

	X-ray data						Optical/UV and X-ray data					
Date MJD	k [10^{-28}]	α ...	β ...	ν_* [Hz]	χ^2 ...	$\nu_{syn,p}$ [10^{17} Hz]	k [10^{-28}]	α ...	β ...	ν_* [Hz]	χ^2 ...	$\nu_{syn,p}$ [10^{16} Hz]
typical	1.259	–1.575	0.274	2.173×10^{12}	0.007	1.086	1.000	–1.533	0.172	1.309×10^{9}	0.008	3.022
55265	1.000	–1.785	0.527	1.622×10^{15}	0.002	7.118	7.079	–1.412	0.221	4.721×10^{11}	0.024	13.52
55266	1.000	–1.802	0.490	8.279×10^{14}	0.002	5.987	1.000	–1.692	0.227	1.358×10^{11}	0.015	11.55
55267	0.832	–1.494	0.244	2.512×10^{12}	0.001	3.241	1.000	–1.447	0.157	1.791×10^{9}	0.002	11.12
55268	1.000	–1.708	0.414	2.541×10^{14}	0.001	4.737	1.000	–1.672	0.218	7.129×10^{10}	0.009	9.582
55269	1.000	–1.688	0.385	1.327×10^{14}	0.001	4.111	1.000	–1.636	0.209	4.645×10^{10}	0.007	9.402
55270	1.000	–1.556	0.237	5.035×10^{11}	0.004	1.243	1.000	–1.512	0.171	2.606×10^{9}	0.003	5.768
55271	1.000	–1.678	0.284	2.786×10^{12}	0.003	1.445	1.000	–1.660	0.214	3.837×10^{10}	0.003	6.294
55272	1.000	–1.778	0.434	1.563×10^{14}	0.002	2.480	1.778	–1.745	0.275	6.166×10^{11}	0.010	6.038
55273	1.000	–1.774	0.450	1.905×10^{14}	0.002	2.303	1.000	–1.757	0.248	1.297×10^{11}	0.007	4.693
55274	1.000	–1.499	0.268	3.631×10^{12}	0.001	1.668	1.000	–1.495	0.166	1.377×10^{9}	0.003	4.509
55275	1.000	–1.602	0.271	1.730×10^{12}	0.003	1.093	1.000	–1.539	0.177	2.858×10^{9}	0.005	4.249
55276	1.000	–1.481	0.220	3.311×10^{11}	0.003	1.441	0.794	–1.455	0.146	2.265×10^{8}	0.003	5.788
55277	2.667	–1.411	0.299	1.578×10^{13}	0.008	1.697	1.000	–1.560	0.182	3.972×10^{9}	0.006	4.285

Notes: [a] Note-The fitting is obtained by considering the photon energy ν to be the independent variable. Transforming the log-parabolic model into $\log\nu - \log\nu F_\nu$ space, we can obtain a relation $\log\nu F_\nu = c_0 + c_1\log\nu + c_2(\log\nu)^2$, where $c_0 = -\beta(\log\nu_*)^2 + \alpha\log\nu_* + \log k$, $c_1 = 2\beta\log\nu_* - \alpha + 1$ and $c_2 = -\beta$. The parameters c_1 and c_2 can localize the synchrotron SED peak by $\nu_{\mathrm{syn,p}} = -c_1/(2c_2)$.

chrotron SED component applying a reasonably smooth interpolation or extrapolation model (e.g., Massaro et al. 2004; Błażejowski et al. 2005; Tramacere et al. 2009; Ushio et al. 2010). We introduce a log-parabolic model with

$$F(\nu) = k\left(\frac{\nu}{\nu_*}\right)^{-\alpha-\beta\log(\nu/\nu_*)} \qquad (32)$$

in the $\nu - F(\nu)$ space (e.g., Baloković et al. 2016). We utilize the model to fit to the X-ray data alone, and to both the ultraviolet (UV)/optical and X-ray data. In this model, α and β are free parameters, while ν_* is a fixed parameter at which α equals the local power-law photon index. The β parameter exhibits deviation of the spectral slope away from ν_*. The evolution of the peak frequency of the synchrotron SED component in the observed epoch is reported in Table 2. The corresponding peak frequencies of the synchrotron SED component for each activity are plotted in Figure 3. The plot includes a comparison of both the electric field and the magnetic field strength, the ratio of the electric field and the magnetic field strength, the spectral slopes of synchrotron emission, and the light curve of X-ray and γ-ray. We note that the agreement between the migration in the peak positions of the synchrotron SED component and evolution of the ratio of the electric field and magnetic field strength is excellent during the activity epochs. Since the magnetic field strength in the observation epoch experiences minor changes, and the summation of both the magnetic field and the soft photon field energy density is fixed, we suggest that it is reasonable to conclude that the electrostatic acceleration is responsible for the evolution of the multi-wavelength SED characteristic by shifting the peak frequency. We are interested in comparing the ratio of the electric field and the magnetic field strength with the spectral slopes of synchrotron emission, and the light curve of X-ray and γ-ray. One can find that when the ratio increases, the spectral slopes of synchrotron emission enlarge, and the X-ray and γ-ray fluxes strengthen. These are a consequence of the electrostatic acceleration in an electric field tending to harden the particle distribution,

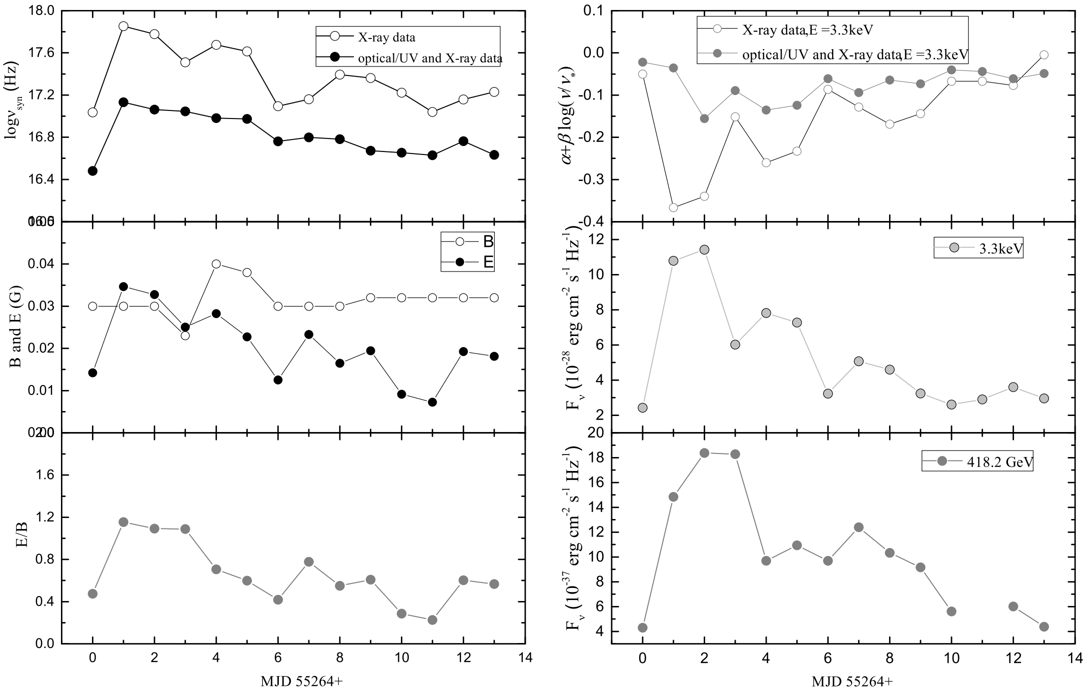

Fig. 3 *Left panels*: Temporal evolution of the peak frequency of the synchrotron SED component (*top panel*), both the electric field and the magnetic field strength (*middle panel*), and the ratio of the electric field and the magnetic field strength (*bottom panel*) during the 13-day flaring event in March 2010 of Mrk 421; *Right panels*: Temporal evolution of the spectral slopes of synchrotron emission (*top panel*), and the X-ray (*middle panel*) and γ-ray (*bottom panel*) fluxes during the 13-day flaring event in March 2010 of Mrk 421. The peak location of the synchrotron SED component is estimated by fitting a log-parabolic model in Eq. (31). The associated ratio of the electric field and the magnetic field strength is computed using the model parameters. The plot assumes the typical state at the epoch of MJD 55264. We note that the γ-ray fluxes are absent from observation in the day of MJD 55275.

which enhances the high-energy component of resulting synchrotron emission spectrum.

6 CONCLUSIONS AND DISCUSSION

It is believed that determining the jet microphysics from the SED of a blazar is a challenging problem of inversion. In a phenomenological view, it is interesting and important to find the exclusive characteristic of the emission energy spectrum for tracing the jet microphysics. The present paper introduces a linear acceleration by integrating the reconnection electric field into the particle transport model which has been proposed by Zheng et al. (2019). We expected to find observed evidence for the electrostatic acceleration in the blazar jet. In the model, the ratio of the electric field and the magnetic field strength reflecting the electrostatic acceleration rate is established. On the basis of the model's expected maximum Lorentz factor, we deduce the maximum photon energy of the synchrotron peak in the SSC model frame. The result indicates that the energy of the synchrotron peak depends on the ratio of the electric field and the magnetic field strength. In order to justify the migration in the peak positions of the synchrotron SED component, we test the theoretical SED effects of changes in the parameters. The tests provide strong evidence for the evolution of multi-wavelength SED characteristic by shifting the peak frequency, with an accompanying orphan flare at the X-ray and GeV-TeV γ-ray bands. These results provide an important electrostatic acceleration diagnostic in blazar jets. Assuming suitable model parameters, we apply the results of the simulation to the 13-day flaring event in March 2010 of Mrk 421, concentrating on the evolution of the multi-wavelength SED characteristic by shifting the peak frequency. It is clear that the ratio of the electric field and the magnetic field strength plays an important role in the temporal evolution of the peak frequency of the synchrotron SED component. Therefore, we consider it reasonable to suggest the electrostatic acceleration is responsible for the evolution of multi-wavelength SED characteristic by shifting the peak frequency.

Phenomenologically, the model effort of Aleksić et al. (2015) for the 13 consecutive day activities of Mrk 421 focuses on the correlated variability at the X-ray and γ-

ray bands without variability in the optical/UV bands. Their model paradigm confirms that the one-zone SSC model can describe the SED on each day reasonably well. Alternatively, the flaring activity can be reproduced by a two-zone SSC model, where one zone is responsible for the quiescent emission, and the other zone contributes to the daily variable emission occurring at X-ray and γ-ray bands (Aleksić et al. 2015). In the context model, we concentrate on the evolution of the multi-wavelength SED characteristic by shifting the peak frequency. To render the nonlinear effect of SSC process, we assume a constant soft photon field instead of the synchrotron emission field. With the adopted parameters $B = 0.03$ G, it results in $u_B \sim 3.6 \times 10^{-5}$ erg cm^{-3}. Based on the model results, we can also estimate the synchrotron emission field $u_{syn} \sim 10^{-4}$ erg cm^{-3}. If we directly include the synchrotron emission field into the transport equation, we find $u = u_B + u_{syn} \sim 10^{-4}$ erg cm^{-3}. This value is five orders of magnitude less than the constant soft photon field of the model assumed with $u = 25.38$ erg cm^{-3}. It is believed that a lower soft photon field results in larger equilibrium Lorentz factor. The calculated synchrotron emission field induces the equilibrium Lorentz factor γ_e around $10^7 \sim 10^8$. This is far from the equilibrium Lorentz factor that is required by the observed synchrotron peak energy. In order to obtain a corresponding synchrotron peak energy, we assume a large value for soft photon fields to establish the particle distributions. It is important to assume a plane shock front propagating along a cylindrical jet. A particle energy distribution is shaped by experiencing acceleration, cooling, injection and escape processes around the shock front, and subsequently drifts away into the downstream flow, in which it emits most of its energy. Since the context introduces a shock-induced magnetic reconnection scenario, we must emphasize the aim of model assumed soft photon fields is to shape a particle energy distribution around the shock front, whereas the emission spectra are strictly calculated in the frame of SSC process.

In this context, we do not provide detailed insights on what is the dominate acceleration mechanism in the reconnection region. However, it is interesting to find that all of the island contraction (Drake et al. 2006), anti-reconnection between colliding islands (Oka et al. 2010; Sironi & Spitkovsky 2014) and curvature drift acceleration (Guo et al. 2014, 2015) are able to transfer the available magnetic energy into a population of non-thermal ultra-relativistic electrons via the induced large-scale electric field. Actually, the high energy particles are regulated and focused towards the reconnection layer midplane (e.g., Contopoulos 2007). Once the particles are immersed in the layer, they suffer from weak radiative losses, but strong coherent electric fields (Uzdensky et al. 2011). On the contrary, the ambient magnetic field exceeds the electric field in the surrounding region. In this scenario, the layer can be treated as a linear accelerator (Cerutti et al. 2013). Since magnetic reconnections offer natural regions where the electric field is stronger than the magnetic field, we adopt a simple linear acceleration mechanism by the reconnection electric field. On the basis of assuming a constant electric field strength in the region, we propose a possible explanation for the origin of the temporal evolution on the peak frequency of the synchrotron emission SED component.

It is convenient to compare the relative contributions from shock acceleration and electrostatic acceleration in the dissipated region. The model presented in this work suggests the ratio of the electric field and magnetic field strength in a limited range from 0.2 to 1.2 during the activity epochs. Since we adopt the shock acceleration efficiency factor $\xi = 0.1$ in this context, we can conclude that the first-order momentum gain by electrostatic acceleration is a dominant mechanism at the dissipation region in the jet. However, we should emphasize that shock, none the less, plays an important role in regulating escape of the particles, and therefore it is an essential composition in the proposed model, despite the momentum gain by shock acceleration being negligible. Actually, in the environment where the magnetic reconnection is efficient, so as to provide the electric field, the emission region has to be considerably magnetized. There the shock acceleration cannot be efficient, or even the shock can hardly happen (e.g., Kirk et al. 2000; Achterberg et al. 2001). We believe that both shock acceleration and electric field acceleration are unlikely to coexist. We do not propose an explanation for why they are happening in the blazar region. However, it is interesting to speculate that these might be a result of the electric field acceleration concentrating in the comparatively smaller volume surrounding the shock and the shock acceleration occurring around the shock front. In this scenario, the electric field acceleration is best interpreted as a pre-acceleration process in which a fraction of particles obtained energy from the electric field easily trigger a Fermi-type acceleration. Such pre-acceleration process in our steady-state particle spectrum could be simply considered by postulating higher energy for the injected electrons with a Lorentz factor, γ_0.

There are alternative criteria for the blazar classification including the use of the peak frequency of the synchrotron SED component: low synchrotron-peaked blazars (LSP; $\log \nu_{\rm syn,p} < 14$ Hz); intermediate synchrotron-peaked blazars (ISP; 14 Hz $\leq \log \nu_{\rm syn,p} \leq 15$ Hz); and high-synchrotron-peaked blazars (HSP; $\log \nu_{\rm syn,p} > 15$ Hz) (e.g., Padovani & Giommi 1995; Nieppola et al. 2006, 2008; Abdo et al. 2010; Fan et al. 2016). It is surprising to find evidence for the migration in the peak positions of the synchrotron SED component during the activity epochs of Mrk 421. Since most blazars appear as luminous sources characterized by noticeable and rapid flux variability at all observed frequencies, on the basis of the proposed model results, we postulate that the peak frequency of the synchrotron SED component may signify a temporary characteristic of blazars, rather than a permanent one. Taking the finiteness of the sample into account, we defer to this possibility for other blazar sources that are extensively observed.

A potential drawback of the proposed model is that we apply a steady particle distribution instead of time-dependent evolution to model the SEDs each day and estimate physical parameters in the dissipation region. As a result, it provides an estimation of the temporal evolution of these physical parameters, but we cannot simulate the light curves during the activity epochs. Consequently, the expected orphan flare at the X-ray and GeV-TeV γ-ray bands cannot be generated by the proposed model in the context. On the other hand, in spite that we introduce an ambient soft photon field to establish the particle distributions, the theoretical photon spectra reproducing the SSC process results in the proposed model not being able to explain the pure orphan γ-ray flare. In order to interpret the flares, MacDonald et al. (2015) proposed the *Ring of Fire* model, where the electrons in the blob up-scatter the ring photons to simulate the origin of orphan γ-ray flares from the jet dissipation region. Alternatively, the hadronic model has been proposed in which either the proton-synchrotron emission or the photohadronic process can explain orphan high energy flares (Cerruti et al. 2015; Sahu et al. 2019). In the current context, while the special variability timescale does not need to be taken into account, the snapshot approach with the steady SSC model allows us to investigate the temporary evolution of basic physical parameters averaged over a day; this can consider the blobs independently of the difficulties associated with a time dependent model. As time dependent variations of electric and magnetic fields (e.g., Kroon et al. 2018, 2019) can result in the evolution of the emission electrons, we leave this issue for our future work.

Acknowledgements We thank the anonymous referee for valuable comments and suggestions. This work was partially supported by the National Natural Science Foundation of China (Grant Nos. 11673060, 11763005, 11873043 and 11991051), the Specialized Research Fund for Shandong Provincial Key Laboratory (Grant No. KLWH201804), and the Research Foundation for Scientific Elitists of the Department of Education of Guizhou Province (Grant No. QJHKYZ[2018]068).

References

Abdo, A. A., Ackermann, M., Agudo, I., et al. 2010, ApJ, 716, 30
Abdo, A. A., Ackermann, M., Ajello, M., et al. 2011, ApJ, 736, 131
Abeysekara, A. U., Archambault, S., Archer, A., et al. 2017, ApJ, 834, 2
Achterberg, A., Gallant, Y. A., Kirk, J. G., & Guthmann, A. W. 2001, MNRAS, 328, 393
Ahnen, M. L., Ansoldi, S., Antonelli, L. A., et al. 2018, A&A, 620, A181
Aleksić, J., Ansoldi, S., Antonelli, L. A., et al. 2015, A&A, 578, A22
Asano, K., & Hayashida, M. 2015, ApJL, 808, L18
Baloković, M., Paneque, D., Madejski, G., et al. 2016, ApJ, 819, 156
Baring, M. G., Böttcher, M., & Summerlin, E. J. 2017, MNRAS, 464, 4875
Begelman, M. C. 1998, ApJ, 493, 291
Bell, A. R. 1978, MNRAS, 182, 147
Beniamini, P., & Giannios, D. 2017, MNRAS, 468, 3202
Beniamini, P., & Granot, J. 2016, MNRAS, 459, 3635
Beniamini, P., & Piran, T. 2013, ApJ, 769, 69
Blandford, R. D., & Königl, A. 1979, ApJ, 232, 34
Błażejowski, M., Blaylock, G., Bond, I. H., et al. 2005, ApJ, 630, 130
Bloom, S. D., & Marscher, A. P. 1996, ApJ, 461, 657
Böttcher, M., & Chiang, J. 2002, ApJ, 581, 127
Camenzind, M., & Krockenberger, M. 1992, A&A, 255, 59
Celotti, A., Maraschi, L., & Treves, A. 1991, ApJ, 377, 403
Cerruti, M., Zech, A., Boisson, C., & Inoue, S. 2015, MNRAS, 448, 910
Cerutti, B., & Philippov, A. A. 2017, A&A, 607, A134
Cerutti, B., Werner, G. R., Uzdensky, D. A., & Begelman, M. C. 2012, ApJL, 754, L33
Cerutti, B., Werner, G. R., Uzdensky, D. A., & Begelman, M. C. 2013, ApJ, 770, 147
Chiaberge, M., & Ghisellini, G. 1999, MNRAS, 306, 551
Christie, I. M., Petropoulou, M., Sironi, L., & Giannios, D. 2019, MNRAS, 482, 65
Contopoulos, I. 2007, A&A, 472, 219
de Vaucouleurs, G., de Vaucouleurs, A., Corwin, Herold G., J., et al. 1991, Third Reference Catalogue of Bright Galaxies
Dermer, C. D., Schlickeiser, R., & Mastichiadis, A. 1992, A&A, 256, L27
Drake, J. F., Swisdak, M., Che, H., & Shay, M. A. 2006, Nature, 443, 553
Drury, L. 1983, Space Sci. Rev., 36, 57
Dwek, E., & Krennrich, F. 2005, ApJ, 618, 657
Eichler, D. 1993, ApJ, 419, 111
Fan, J. H., Yang, J. H., Liu, Y., et al. 2016, ApJS, 226, 20
Finke, J. D., Razzaque, S., & Dermer, C. D. 2010, ApJ, 712, 238
Fossati, G., Maraschi, L., Celotti, A., Comastri, A., & Ghisellini,

G. 1998, MNRAS, 299, 433
Franceschini, A., Rodighiero, G., & Vaccari, M. 2008, A&A, 487, 837
Ghisellini, G., Celotti, A., & Costamante, L. 2002, A&A, 386, 833
Ghisellini, G., & Maraschi, L. 1989, ApJ, 340, 181
Ghisellini, G., Maraschi, L., Tanzi, E. G., & Treves, A. 1986, ApJ, 310, 317
Giannios, D. 2013, MNRAS, 431, 355
Giannios, D., & Spruit, H. C. 2006, A&A, 450, 887
Giannios, D., Uzdensky, D. A., & Begelman, M. C. 2009, MNRAS, 395, L29
Giannios, D., Uzdensky, D. A., & Begelman, M. C. 2010, MNRAS, 402, 1649
Giebels, B., Dubus, G., & Khélifi, B. 2007, A&A, 462, 29
Gopal-Krishna, & Wiita, P. J. 1992, A&A, 259, 109
Guo, F., Li, H., Daughton, W., & Liu, Y.-H. 2014, Phys. Rev. Lett., 113, 155005
Guo, F., Liu, Y.-H., Daughton, W., & Li, H. 2015, ApJ, 806, 167
Jones, T. W., O’dell, S. L., & Stein, W. A. 1974, ApJ, 188, 353
Kagan, D., Nakar, E., & Piran, T. 2018, MNRAS, 476, 3902
Kataoka, J., & Stawarz, Ł. 2016, ApJ, 827, 55
Katarzyński, K., Ghisellini, G., Mastichiadis, A., Tavecchio, F., & Maraschi, L. 2006, A&A, 453, 47
Katarzyński, K., Sol, H., & Kus, A. 2001, A&A, 367, 809
Kirk, J. G., Guthmann, A. W., Gallant, Y. A., & Achterberg, A. 2000, ApJ, 542, 235
Kirk, J. G., Rieger, F. M., & Mastichiadis, A. 1998, A&A, 333, 452
Kirk, J. G., & Skjæraasen, O. 2003, ApJ, 591, 366
Kneiske, T. M., Bretz, T., Mannheim, K., & Hartmann, D. H. 2004, A&A, 413, 807
Kneiske, T. M., Mannheim, K., & Hartmann, D. H. 2002, A&A, 386, 1
Krawczynski, H., Hughes, S. B., Horan, D., et al. 2004, ApJ, 601, 151
Kroon, J. J., Becker, P. A., & Finke, J. D. 2018, ApJ, 853, 16
Kroon, J. J., Becker, P. A., & Finke, J. D. 2019, ApJ, 872, 65
Kroon, J. J., Becker, P. A., Finke, J. D., & Dermer, C. D. 2016, ApJ, 833, 157
Lewis, T. R., Becker, P. A., & Finke, J. D. 2016, ApJ, 824, 108
MacDonald, N. R., Marscher, A. P., Jorstad, S. G., & Joshi, M. 2015, ApJ, 804, 111
Marscher, A. P. 2014, ApJ, 780, 87
Marscher, A. P., & Gear, W. K. 1985, ApJ, 298, 114
Massaro, E., Perri, M., Giommi, P., & Nesci, R. 2004, A&A, 413, 489
Mastichiadis, A., & Kirk, J. G. 1997, A&A, 320, 19
Mastichiadis, A., & Moraitis, K. 2008, A&A, 491, L37
Nalewajko, K., Giannios, D., Begelman, M. C., Uzdensky, D. A., & Sikora, M. 2011, MNRAS, 413, 333
Nalewajko, K., Sikora, M., Madejski, G. M., et al. 2012, ApJ, 760, 69
Narayan, R., & Piran, T. 2012, MNRAS, 420, 604
Nieppola, E., Tornikoski, M., & Valtaoja, E. 2006, A&A, 445, 441
Nieppola, E., Valtaoja, E., Tornikoski, M., et al. 2008, A&A, 488, 867
Oka, M., Phan, T. D., Krucker, S., et al. 2010, ApJ, 714, 915
Padovani, P., & Giommi, P. 1995, ApJ, 444, 567
Petropoulou, M. 2014, A&A, 571, A83
Petropoulou, M., Giannios, D., & Sironi, L. 2016, MNRAS, 462, 3325
Petrosian, V., & Liu, S. 2004, ApJ, 610, 550
Philippov, A. A., & Spitkovsky, A. 2014, ApJL, 785, L33
Raiteri, C. M., Villata, M., Acosta-Pulido, J. A., et al. 2017, Nature, 552, 374
Rani, B., Krichbaum, T. P., Fuhrmann, L., et al. 2013, A&A, 552, A11
Razzaque, S., Dermer, C. D., & Finke, J. D. 2009, ApJ, 697, 483
Romanova, M. M., & Lovelace, R. V. E. 1992, A&A, 262, 26
Rybicki, G. B., & Lightman, A. P. 1979, Radiative processes in astrophysics
Sahu, S., López Fortín, C. E., & Nagataki, S. 2019, ApJL, 884, L17
Schlickeiser, R. 1985, A&A, 143, 431
Schlickeiser, R. 1989, ApJ, 336, 243
Sikora, M., Błażejowski, M., Begelman, M. C., & Moderski, R. 2001, ApJ, 554, 1
Sironi, L., & Spitkovsky, A. 2014, ApJL, 783, L21
Stecker, F. W., de Jager, O. C., & Salamon, M. H. 1992, ApJL, 390, L49
Stecker, F. W., Malkan, M. A., & Scully, S. T. 2006, ApJ, 648, 774
Tramacere, A., Giommi, P., Perri, M., Verrecchia, F., & Tosti, G. 2009, A&A, 501, 879
Urry, C. M. 1998, Advances in Space Research, 21, 89
Urry, C. M., & Padovani, P. 1995, PASP, 107, 803
Ushio, M., Stawarz, Ł., Takahashi, T., et al. 2010, ApJ, 724, 1509
Uzdensky, D. A., Cerutti, B., & Begelman, M. C. 2011, ApJL, 737, L40
Weidinger, M., & Spanier, F. 2015, A&A, 573, A7
Werner, G. R., & Uzdensky, D. A. 2017, ApJL, 843, L27
Zhang, B., & Zhang, B. 2014, ApJ, 782, 92
Zheng, Y. G., Kang, S. J., Yang, C. Y., & Bai, J. M. 2019, ApJ, 873, 7
Zheng, Y. G., Long, G. B., Yang, C. Y., & Bai, J. M. 2018, MNRAS, 478, 3855
Zheng, Y. G., & Yang, C. Y. 2016, MNRAS, 457, 3535
Zheng, Y. G., Yang, C. Y., Zhang, L., & Wang, J. C. 2017, ApJS, 228, 1
Zheng, Y. G., & Zhang, L. 2011, ApJ, 728, 105